Journal of Fluid Mechanics
http://journals.cambridge.org/FLM

Additional services for ***Journal of Fluid Mechanics:***

Email alerts: Click here
Subscriptions: Click here
Commercial reprints: Click here
Terms of use : Click here

On the liquid lining in fluid-conveying curved tubes

Andrew L. Hazel, Matthias Heil, Sarah L. Waters and James M. Oliver

Journal of Fluid Mechanics / Volume 705 / August 2012, pp 213 - 233
DOI: 10.1017/jfm.2011.346, Published online: 29 September 2011

Link to this article: http://journals.cambridge.org/abstract_S0022112011003466

How to cite this article:
Andrew L. Hazel, Matthias Heil, Sarah L. Waters and James M. Oliver (2012). On the liquid lining in fluid-conveying curved tubes. Journal of Fluid Mechanics,705, pp 213-233 doi:10.1017/jfm.2011.346

Request Permissions : Click here

CAMBRIDGE JOURNALS

Downloaded from http://journals.cambridge.org/FLM, IP address: 130.88.16.106 on 17 Aug 2012

J. Fluid Mech. (2012), *vol.* 705, *pp.* 213–233. © Cambridge University Press 2011
doi:10.1017/jfm.2011.346

On the liquid lining in fluid-conveying curved tubes

Andrew L. Hazel[1]†, Matthias Heil[1], Sarah L. Waters[2] and James M. Oliver[2]

[1] School of Mathematics, University of Manchester, Oxford Road, Manchester M13 9PL, UK

[2] OCIAM, Mathematical Institute, University of Oxford, 24-29 St Giles, Oxford OX1 3LB, UK

(Received 3 May 2011; revised 29 July 2011; accepted 10 August 2011;
first published online 29 September 2011)

We consider axially uniform, two-phase flow through a rigid curved tube in which a fluid (air) core is surrounded by a film of a second, immiscible fluid (water): a simplified model for flow in a conducting airway of the lung. Jensen (1997) showed that, in the absence of a core flow, surface tension drives the system towards a configuration in which the film thickness tends to zero on the inner wall of the bend. In the present work, we demonstrate that the presence of a core flow, driven by a steady axial pressure gradient, allows the existence of steady states in which the film thickness remains finite, a consequence of the fact that the tangential stresses at the interface, imposed by secondary flows in the core, can oppose the surface-tension-driven flow. For sufficiently strong surface tension, the steady configurations are symmetric about the plane containing the tube's centreline, but as the surface tension decreases the symmetry is lost through a pitchfork bifurcation, which is closely followed by a limit point on the symmetric solution branch. This solution structure is found both in simulations of the Navier–Stokes equations and a thin-film model appropriate for weakly curved tubes. Analysis of the thin-film model reveals that the bifurcation structure arises from a perturbation of the translational degeneracy of the interface location in a straight tube.

Key words: pulmonary fluid mechanics, thin films

1. Introduction

The bifurcating network of airways in the lung is lined with a liquid film that serves to protect and hydrate the airway epithelium and is also involved in various mechanisms for the removal of foreign particles. The effective biological function of the lining depends on its distribution throughout the airways, which is influenced by surface tension at the air–liquid interface and the geometry of the airways. Understanding the respective roles of these physical influences is, therefore, important in order to obtain a complete understanding of the physiology and pathology of the lung.

For a straight tube of circular cross-section in the absence of gravity, a static, uniform film is a trivial equilibrium configuration. However, this solution has a translational degeneracy because the circular interface can be located anywhere

† Email address for correspondence: Andrew.Hazel@manchester.ac.uk

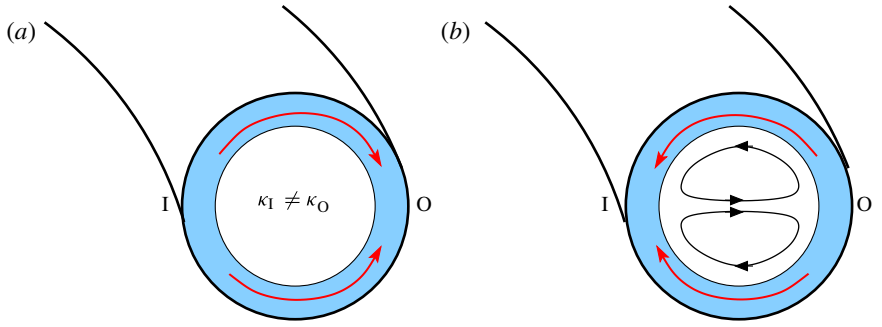

FIGURE 1. (Colour online available at journals.cambridge.org/flm) Principal mechanisms driving axially uniform flows within a liquid film that surrounds an air core in a curved tube: (*a*) differences in mean interface curvature between the regions near the inner (I) and outer (O) wall of the curved tube drive a surface-tension-induced flow towards the outer wall; (*b*) secondary flows in the core drive a flow towards the inner wall.

within the tube's cross-section. The introduction of centreline curvature breaks the degeneracy, but in general a uniform film is no longer an equilibrium state: if the tube's centreline is curved, the mean curvature of an air–liquid interface bounding a film of constant thickness varies around the perimeter within the tube's cross-section. Assuming a constant air (core) pressure, the corresponding surface-tension-induced pressure gradient within the fluid film drives a flow towards the outer wall of the bend: see figure 1(*a*). Hence, the air core moves towards the inner wall. Jensen (1997) considered the evolution of a thin film of incompressible Newtonian fluid that lines a uniform, weakly curved circular tube, and showed that the film approaches a 'dry spot' solution in infinite time. In the late stages of the evolution, the inner wall remains wet and is covered by a vanishingly thin fluid layer, while a near-equilibrium lobe forms on the outer wall. Jensen's study neglected the influence of any air flow on the liquid film, however.

In general, axially uniform flow, driven by a steady pressure gradient along a curved tube, is accompanied by secondary flow within the tube's cross-section, and Dean (1928) determined the direction of the secondary flows across the centre of the tube to be from the inner to the outer wall of the bend (irrespective of the direction of the axial flow), as shown in figure 1(*b*). The secondary flows within the air core exert a tangential shear stress on the air–liquid interface in the cross-sectional plane, which drives the lining fluid towards the inner wall of the bend. The redistribution of a thin liquid film by azimuthal shear stresses in a straight tube was considered by Band *et al.* (2009). They showed that for a prescribed interfacial shear-stress distribution corresponding to the secondary flows calculated by Dean (1928), an initially uniform film of incompressible Newtonian fluid also approaches a 'dry spot' solution in infinite time; but in this case, the lobe forms on what would be the inner wall.

In the present contribution, we consider the interaction of these two competing mechanisms by considering the fully developed, co-axial flow of two incompressible, immiscible, Newtonian fluids through a uniformly curved tube. We formulate the general problem in § 2.1 in terms of two Navier–Stokes equations coupled by a common interface. In § 2.2 we also derive a simplified evolution equation for the thickness of the fluid film in the limit in which the film is thin and the curvature of the tube is weak. In § 3, we present results from numerical simulations of the

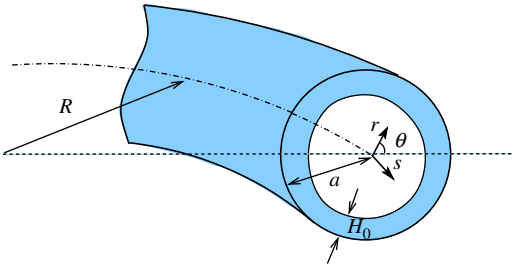

FIGURE 2. (Colour online) Sketch of the problem: a uniformly curved tube has a circular cross-section of radius a and contains a layer of incompressible Newtonian fluid of thickness H_0 surrounding a core that consists of a second immiscible, incompressible Newtonian fluid. The tube's centreline is planar and has a radius of curvature R. A curvilinear coordinate system is defined by plane polar coordinates (r, θ) within the tube's cross-section and an axial coordinate s along the tube's centreline.

system of coupled Navier–Stokes equations for a set of parameters, appropriate for the tenth-generation conducting airways of the lung. In § 4, we demonstrate that the thin-film model reproduces the salient features of the system and use it to examine the origin of the observed behaviour in detail. Finally, we draw our conclusions in § 5.

2. The model

We consider the co-axial flow of two immiscible, incompressible Newtonian fluids within a curved tube of radius a whose centreline is planar and has curvature $1/R$. An inner (core) fluid (fluid 1) is surrounded by a film of an outer fluid (fluid 2) as shown in figure 2. The flow is driven by a constant pressure gradient G^* along the curved tube. In what follows, subscripts will be used to distinguish the two fluids and a superscript * will be used to indicate dimensional quantities, as opposed to their dimensionless equivalents, where required. Throughout this paper we neglect the influence of gravity and assume that the flow is fully developed so that the fluid velocities and the pressure gradient are independent of the axial coordinate.

2.1. *Navier–Stokes model*

We denote the velocities and pressures in the two fluids by $\boldsymbol{u}_i^*$ and p_i^*, respectively, and assume that the interface between the two fluids (of mean curvature κ^*) is parametrised by a time-dependent position vector, $\boldsymbol{r}^*$. We non-dimensionalise all quantities using the density and viscosity of the core fluid, ρ_1 and μ_1, respectively, the magnitude of the imposed pressure gradient, G^*, and the tube radius, a. Thus, $\boldsymbol{r}^* = a\,\boldsymbol{r}$, $p_i^* = G^* a\, p_i$, $\boldsymbol{u}_i^* = (G^* a^2/\mu_1)\,\boldsymbol{u}_i$, $\kappa^* = (1/a)\,\kappa$, and we non-dimensionalise time by $t^* = (\mu_1/(G^* a))\,t$.

The flow in each of the two fluids is then governed by the non-dimensional Navier–Stokes equations

$$\frac{\rho_i}{\rho_1} Re \left(\frac{\partial \boldsymbol{u}_i}{\partial t} + \boldsymbol{u}_i \cdot \boldsymbol{\nabla} \boldsymbol{u}_i \right) = \hat{\boldsymbol{s}} - \boldsymbol{\nabla} p_i + \frac{\mu_i}{\mu_1} \nabla^2 \boldsymbol{u}_i, \quad \boldsymbol{\nabla} \cdot \boldsymbol{u}_i = 0, \tag{2.1}$$

where we have introduced the driving pressure gradient as a body force, acting in the direction of the unit vector $\hat{\boldsymbol{s}}$ along the tube's curved centreline.

The flow is subject to a no-slip boundary condition, $\boldsymbol{u}_2 = \boldsymbol{0}$, at the tube wall. At the interface we impose the continuity of velocity, as well as the kinematic and dynamic

boundary conditions,

$$\boldsymbol{u}_1 = \boldsymbol{u}_2, \tag{2.2}$$

$$\boldsymbol{u}_1 \cdot \hat{\boldsymbol{n}} = \frac{\partial \boldsymbol{r}}{\partial t} \cdot \hat{\boldsymbol{n}}, \tag{2.3}$$

$$(\boldsymbol{\Sigma}_1 - \boldsymbol{\Sigma}_2) \cdot \hat{\boldsymbol{n}} = \frac{\kappa}{Ca}\hat{\boldsymbol{n}}, \tag{2.4}$$

where $\hat{\boldsymbol{n}}$ is a unit vector normal to the interface and directed into the core, and the non-dimensional stress tensors $\boldsymbol{\Sigma}_i = \boldsymbol{\Sigma}_i^*/(G^* a)$ are defined by

$$\boldsymbol{\Sigma}_i = -p_i \mathrm{I} + \frac{\mu_i}{\mu_1}\left[\boldsymbol{\nabla}\boldsymbol{u}_i + (\boldsymbol{\nabla}\boldsymbol{u}_i)^{\mathrm{T}}\right]. \tag{2.5}$$

The governing parameters are the Reynolds number $Re = \rho_1 G^* a^3/\mu_1^2$, which is a dimensionless measure of the driving pressure gradient; the capillary number $Ca = G^* a^2/\gamma$, which reflects the magnitude of the driving pressure gradient (and hence secondary flows) relative to the constant surface tension, γ, of the interface; and the ratios of physical properties of the two fluids: the viscosity ratio μ_2/μ_1 and the density ratio ρ_2/ρ_1. The curvature ratio $\delta = a/R$ enters the problem through the domain geometry.

2.2. *Thin-film model*

Under normal physiological conditions, the liquid lining in the pulmonary airways is relatively thin and so we shall also employ a thin-film model to describe its evolution. Suppose the typical thickness of the lining fluid is H_0. We define $\epsilon = H_0/a$, and consider the case where $0 < \epsilon \ll 1$. In the absence of both centreline curvature and the core fluid, the dimensional time scale, $\mathscr{T}^*$, governing the film rearrangement follows from a balance between the azimuthal viscous shear stress gradient of $O(\mu_2 \mathscr{U}/(a^2\epsilon^2))$, and the driving azimuthal pressure gradient of $O(\epsilon\gamma/a^2)$, where the velocity scale is given by $\mathscr{U} = a/\mathscr{T}^*$. Hence, $\mathscr{T}^* = 3\mu_2 a/(\epsilon^3\gamma)$ (where the factor of 3 is introduced for later convenience). In terms of the non-dimensionalisations given in § 2.1, the appropriate dimensionless time scale is $\mathscr{T} = (G^* a/\mu_1)\mathscr{T}^* = 3Ca\mu_2/(\epsilon^3\mu_1)$. We set $t = \mathscr{T}\bar{t}$ and assume that $\mathscr{T} \gg 1$ in the analysis that follows.

We choose a curvilinear coordinate system (r, θ, s), where (r, θ) are polar coordinates in the plane of cross-section and s is the distance along the centreline, as shown in figure 2. The origin of the polar coordinate system is located on the tube's centreline and $\theta = 0$ is chosen to correspond to the outer wall of the bend; again see figure 2. We denote the fluid velocity components in the directions of the unit vectors $(\hat{\boldsymbol{r}}, \hat{\boldsymbol{\theta}}, \hat{\boldsymbol{s}})$ by (U_i, V_i, W_i), respectively, and the pressure by P_i $(= p_i)$. The interfacial position is given by $r = 1 - \epsilon\overline{H}(\theta, t)$, and $\overline{H}$ is assumed to be of $O(1)$. To derive an evolution equation for the interfacial position, we make the further assumption that the tube is weakly curved ($\delta \ll 1$) and then solve for the flows in both the core and thin film in turn, coupling them via the interfacial boundary conditions.

2.2.1. *Core-fluid governing equations*

Assuming fully developed flow in a weakly curved tube, we neglect terms of $O(\delta)$ in the Navier–Stokes equations, but assume that $\delta\, Re$ remains finite as $\delta \to 0$. These standard assumptions lead to retention of the centrifugal force terms (proportional to W_1^2) at leading order in the radial and azimuthal equations below ((2.7) and (2.8)), which drive the secondary flows. The governing equations in the core are

then (Pedley 1980)

$$\frac{\partial U_1}{\partial r} + \frac{U_1}{r} + \frac{1}{r}\frac{\partial V_1}{\partial \theta} = 0, \tag{2.6}$$

$$Re\left(\frac{1}{\mathscr{T}}\frac{\partial U_1}{\partial \bar{t}} + U_1\frac{\partial U_1}{\partial r} + \frac{V_1}{r}\frac{\partial U_1}{\partial \theta} - \frac{V_1^2}{r} - \delta\, W_1^2\cos\theta\right)$$
$$= -\frac{\partial P_1}{\partial r} - \frac{1}{r}\frac{\partial}{\partial \theta}\left(\frac{1}{r}\left(V_1 + r\frac{\partial V_1}{\partial r} - \frac{\partial U_1}{\partial \theta}\right)\right), \tag{2.7}$$

$$Re\left(\frac{1}{\mathscr{T}}\frac{\partial V_1}{\partial \bar{t}} + U_1\frac{\partial V_1}{\partial r} + \frac{V_1}{r}\frac{\partial V_1}{\partial \theta} + \frac{U_1 V_1}{r} + \delta\, W_1^2\sin\theta\right)$$
$$= -\frac{1}{r}\frac{\partial P_1}{\partial \theta} + \frac{\partial}{\partial r}\left(\frac{1}{r}\left(V_1 + r\frac{\partial V_1}{\partial r} - \frac{\partial U_1}{\partial \theta}\right)\right), \tag{2.8}$$

$$Re\left(\frac{1}{\mathscr{T}}\frac{\partial W_1}{\partial \bar{t}} + U_1\frac{\partial W_1}{\partial r} + \frac{V_1}{r}\frac{\partial W_1}{\partial \theta} + \delta\, W_1(U_1\cos\theta - V_1\sin\theta)\right)$$
$$= 1 + \frac{1}{r}\frac{\partial}{\partial r}\left(r\frac{\partial W_1}{\partial r}\right) + \frac{1}{r^2}\frac{\partial^2 W_1}{\partial \theta^2}. \tag{2.9}$$

Continuity of velocity at the fluid interface $r = 1 - \epsilon\overline{H}$ implies that, to leading order in ϵ,

$$U_1 = V_1 = W_1 = 0 \quad \text{at } r = 1, \tag{2.10}$$

because the velocity components in the liquid lining are much smaller than those in the core fluid; the liquid-lining velocity scales are given in § 2.2.2 below, and their validity may be confirmed *a posteriori*. Neglecting the time-dependent inertia terms (because $\mathscr{T} \gg 1$), we seek solutions in powers of $\delta\, Re$. The flow in the core is then the standard Dean flow (Dean 1928),

$$U_1 = \frac{\delta\, Re}{2^9 3^2}(1 - r^2)^2(4 - r^2)\cos\theta + \cdots, \tag{2.11}$$

$$V_1 = -\frac{\delta\, Re}{2^9 3^2}\sin\theta(1 - r^2)(4 + 7r^4 - 23r^2) + \cdots, \tag{2.12}$$

$$W_1 = \frac{1}{4}(1 - r^2) + \cdots. \tag{2.13}$$

2.2.2. *Lining-fluid governing equations*

In addition to surface-tension-generated pressure gradients, the flow in the thin film is driven by the tangential stresses at the interface generated by the core flow, and we choose the scale for the velocities in the thin film from the tangential stress balance at the interface. From (2.12) the azimuthal core velocity is of $O(\delta\, Re)$ with corresponding tangential stresses of $O(\mu_1\delta\, Re/a)$. Denoting the azimuthal velocity scale in the thin film by $\mathscr{V}$, the tangential stress is given by $\mu_2\mathscr{V}/(a\epsilon)$ and balancing these stresses gives the azimuthal velocity scale in the thin film as $\mathscr{V} \sim \epsilon\mu_1\delta\, Re/\mu_2$. Similarly, the axial velocity scale is chosen to ensure continuity of tangential stress at the interface and is $\epsilon\mu_1/\mu_2$. The continuity equation then gives the radial velocity scale as $\epsilon^2\mu_1\delta\, Re/\mu_2$. The pressure scale is chosen to ensure a balance between the azimuthal pressure gradient and viscous shear stress, and is $O(\delta Re/\epsilon)$. Motivated by

these considerations, we rescale the variables as follows:

$$r = 1 - \epsilon\bar{r}, \quad (U_2, V_2, W_2) = \frac{\mu_1\epsilon}{\mu_2}(\epsilon\delta\, Re\, \overline{U}_2,\ \delta\, Re\, \overline{V}_2,\ \overline{W}_2), \quad P_2 = \frac{\delta\, Re}{\epsilon}\overline{P}_2. \tag{2.14}$$

We substitute these scalings into the equivalent of (2.6)–(2.9) for the lining fluid, and make the usual lubrication assumption that we can neglect inertia, which corresponds to the reduced Reynolds number (which here is given by $\delta\, Re^2\epsilon^3\mu_1^2/\mu_2^2$) being small (Oron, Davis & Bankoff 1997; Myers 1998). Retaining leading-order terms (with respect to ϵ), the reduced governing equations are then

$$-\frac{\partial\overline{U}_2}{\partial\bar{r}} + \frac{\partial\overline{V}_2}{\partial\theta} = 0, \quad \frac{\partial\overline{P}_2}{\partial\bar{r}} = 0, \quad -\frac{\partial\overline{P}_2}{\partial\theta} + \frac{\partial^2\overline{V}_2}{\partial\bar{r}^2} = 0, \quad \frac{\partial^2\overline{W}_2}{\partial\bar{r}^2} = 0. \tag{2.15a–d}$$

These equations must be solved subject to $\overline{U}_2 = \overline{V}_2 = \overline{W}_2 = 0$ on $\bar{r} = 0$. We must also apply the boundary conditions on the interface, located at $r = 1 - \epsilon\overline{H}$, or $\bar{r} = \overline{H}$. The tangential components of the dynamic boundary condition (2.4) become

$$-\left.\frac{\partial\overline{W}_2}{\partial\bar{r}}\right|_{\bar{r}=\overline{H}} = \left.\frac{\partial W_1}{\partial r}\right|_{r=1}, \quad -\delta\, Re\left.\frac{\partial\overline{V}_2}{\partial\bar{r}}\right|_{\bar{r}=\overline{H}} = r\frac{\partial}{\partial r}\left(\frac{V_1}{r}\right) + \frac{1}{r}\left.\frac{\partial U_1}{\partial\theta}\right|_{r=1}. \tag{2.16a,b}$$

The normal component of the dynamic boundary condition (2.4) gives that

$$\overline{P}_2 = -\frac{1}{128\mathscr{C}}\left(\frac{1}{\epsilon} + \frac{\delta}{\epsilon}\cos\theta + \overline{H} + \frac{\partial^2\overline{H}}{\partial\theta^2}\right) \tag{2.17}$$

where

$$\mathscr{C} = \frac{Ca\,\delta\, Re}{128\epsilon^2}, \tag{2.18}$$

is the thin-film capillary number, and characterises the ratio of viscous effects to surface tension effects (the factor of $1/128$ is introduced for later convenience). Finally, the kinematic condition (2.3) becomes

$$\overline{U}_2 = -\frac{1}{384\mathscr{C}}\frac{\partial\overline{H}}{\partial\bar{t}} - \overline{V}_2\frac{\partial\overline{H}}{\partial\theta} \quad \text{at } \bar{r} = \overline{H}. \tag{2.19}$$

2.2.3. *Thin-film equation*

Equations (2.15*b*,*c*), together with (2.16*b*) and the no-slip condition, give

$$\overline{V}_2 = \frac{1}{2}\frac{\partial\overline{P}_2}{\partial\theta}\bar{r}(\bar{r} - 2\overline{H}) + \frac{1}{192}\bar{r}\sin\theta, \tag{2.20}$$

where $\overline{P}_2$ is given by (2.17). Integrating equation (2.15*a*) with respect to $\bar{r}$ between 0 and $\overline{H}$, applying the no-slip and the kinematic condition (2.19) results in the following evolution equation for the film thickness:

$$\frac{\partial\overline{H}}{\partial\bar{t}} + \frac{\partial\overline{Q}}{\partial\theta} = 0, \tag{2.21}$$

where the flux $\overline{Q}$ is

$$\overline{Q} = \left(-\frac{\delta}{\epsilon}\sin\theta + \frac{\partial\overline{H}}{\partial\theta} + \frac{\partial^3\overline{H}}{\partial\theta^3}\right)\overline{H}^3 + \mathscr{C}\sin\theta\overline{H}^2. \tag{2.22}$$

The terms multiplied by δ/ϵ and $\mathscr{C}$ represent the effects of centreline curvature and the azimuthal shear stresses, respectively.

3. Navier–Stokes simulations

We solve the governing equations (2.1)–(2.4) in an axisymmetric, cylindrical polar coordinate system using an ALE-based finite element method, implemented within the software library `oomph-lib` (Heil & Hazel 2006). The computational domain, the cross-section of the tube, is discretised using $P_2^+P_{-1}$ (Crouzeix–Raviart) triangular elements (see e.g. Gresho & Sani 1998). These elements approximate the velocity components using globally continuous quadratic interpolation, with cubic bubble enrichment on each element to ensure LBB stability (see the discussion in Gresho & Sani 1998, pp. 593–613). We employ a discontinuous, piecewise linear interpolation for the fluid pressure to allow for the pressure jump across the curved interface between the two fluids. The initial mesh is created using Triangle (Shewchuk 1996), followed by an adjustment of the nodal positions to respect the curvilinear boundaries, such that the interface between the two fluids coincides with the edges between adjacent elements. During the computations, the position of the nodes within the finite element mesh is continuously updated by treating the mesh as a pseudo-elastic solid body. The unknown nodal positions are determined by solving the equations of large-displacement elasticity, subject to the kinematic boundary condition (2.3), which is imposed using Lagrange-multiplier-like variables to apply a normal force on the pseudo-solid along the interface; see Cairncross *et al.* (2000).

The choice of discretisation ensures that the kinematic boundary condition (2.3) and the constraint on the continuity of the velocity (2.2) at the interface are automatically satisfied. The dynamic boundary condition (2.4) is directly incorporated into the weak form of the Navier–Stokes equations, and, as usual, we simplify the curvature term via the surface divergence theorem (Ruschak 1980). The flow is enclosed, which means that a reference pressure must be specified, and we set a single pressure value within the fluid film to be zero. In unsteady calculations, conservation of mass ensures that the volume of fluid does not change during the time evolution; it is set by the initial condition. For steady calculations, the volume of fluid contained in the core region (or, equivalently, in the liquid lining) must be imposed explicitly, which is achieved by exploiting the (mathematically equivalent) freedom to specify the value of a pressure at a single point within the core region. We use the volume constraint as the equation that determines the selected pressure value.

In time-dependent simulations the time-derivatives are discretised using a second-order accurate backward differentiation formula (BDF2). After a specified number of time steps, typically two or three, the domain is re-meshed to avoid the occurrence of excessively distorted elements, and the solution is transferred to the new mesh by projection. The size of the elements in the new mesh is guided by error estimates obtained from the ZZ flux-recovery error estimator (Zienkiewicz & Zhu 1992) to ensure that the error remains equipartitioned between the elements, whilst also maintaining element quality.

The algorithm is found to be very robust and allows us to reliably compute a wide range of solutions with film thicknesses down to $O(10^{-3})$. The typical number of elements used is between 2000 and 7000; the greater number of elements is required when the film becomes relatively thin. The accuracy of the computational results was assessed by repeating selected computations using a finer error tolerance in the adaptive remeshing step. This resulted in an approximate doubling of the number of elements but did not change the results to within graphical accuracy. Further validation is provided by the comparisons against the predictions from the thin-film model discussed below.

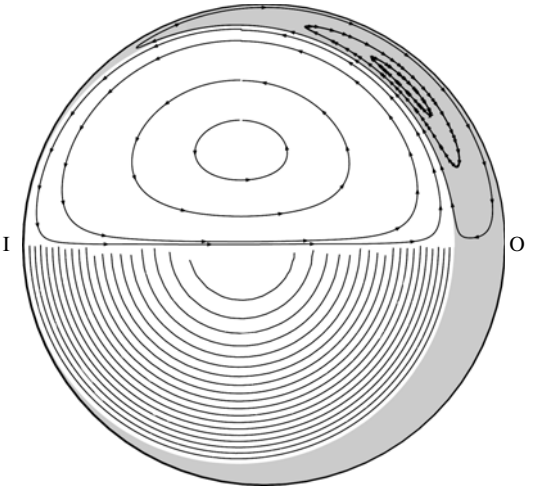

FIGURE 3. Contours of axial velocity (lower half) and secondary-flow streamlines (upper half), computed by direct integration of the velocity field, for the symmetric steady state obtained after time evolution from an initial film thickness $\epsilon = 0.1$ for $Ca = 0.1$, $Re = 100$, $\delta = 0.1$, $\rho_2/\rho_1 = 830$ and $\mu_2/\mu_1 = 55$. The region occupied by the lining fluid is shaded.

3.1. *Parameter values*

We shall concentrate on physical parameters appropriate for the conducting airways of the lungs: an air core surrounded by a film of aqueous liquid. Using physical properties for air and water at a nominal temperature of 20 °C gives $\rho_2/\rho_1 \approx 830$ and $\mu_2/\mu_1 \approx 55$. We present results for a Reynolds number of 100 and a curvature ratio of $\delta = 0.1$, appropriate for an airway in the tenth generation of the lung (Pedley 1977), although we find that the qualitative behaviour of the system is unchanged under variations in δ and Re; see § 3.3. The capillary number $Ca = Re\,\mu_1^2/(\rho_1\gamma a)$, and in a tenth-generation airway $Ca \approx 10^{-5}\,Re$, assuming a surface tension of $\gamma = 7.0 \times 10^{-2}$ N m^{-1}, appropriate for water. The presence of pulmonary surfactant can reduce the surface tension by almost two orders of magnitude, however, giving a nominal range of $10^{-3} < Ca < 10^{-1}$ at $Re = 100$.

3.2. *Results*

Following Jensen (1997), we first consider the system's time evolution from an initial (non-equilibrium) state, in which the fluid is at rest and the lining fluid is contained in a film of uniform thickness $\epsilon = 0.1$, after the impulsive application of the driving axial pressure gradient at $t = 0$. The simulations demonstrate that for sufficiently small values of the capillary number, Ca, the system evolves towards a steady state in which the film thickness remains finite. To obtain the actual steady solution we used the flow field obtained at large times as the initial guess for the solution of the steady equations by Newton's method.

A representative steady solution is illustrated in figure 3, which shows contours of the axial velocity (lower half) and streamlines of the secondary flow (upper half) for a capillary number of $Ca = 0.1$. The secondary flow field is symmetric about the tube's horizontal line of symmetry and the air core is located near the inner bend of the tube. The flow in the air core is approximately the same as the flow in a curved tube with the appropriate (smaller) radius and radius of curvature. Although the boundary condition at the interface is one of tangential slip, rather than no slip, the velocities at the interface between the fluids are sufficiently small that their effect on the flow is

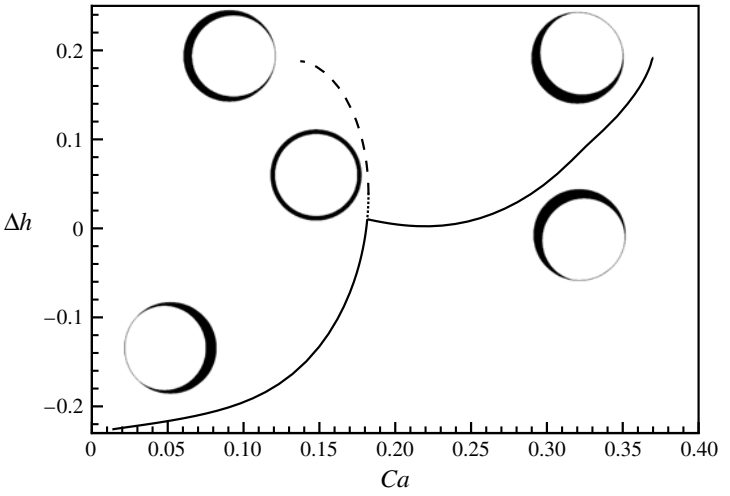

FIGURE 4. Symmetric and asymmetric steady states represented by the difference between the film thickness on the inside ($\theta = \pi$) and outside ($\theta = 0$) of the bend, Δh, plotted against capillary number, Ca. The solid lines denote stable solutions; the dotted line denotes solutions that are stable to symmetric perturbations only; the dashed line denotes solutions that are unstable. Cross-sections of the solution are shown at $Ca = 0.02$ (lower branch), $Ca = 0.18$ (near limit point), $Ca = 0.13$ (upper branch) at $Ca = 0.36$ (asymmetric branch) in which the liquid film is shaded black. The two conjugate solutions are shown at $Ca = 0.36$ and are related by reflection about the horizontal line of symmetry of the cross-section. The other parameters are fixed at $Re = 100$, $\delta = 0.1$, $\epsilon = 0.1$, $\rho_2/\rho_1 = 830$, $\mu_2/\mu_1 = 55$.

minimal. Indeed, (2.10) indicates that the velocities on the interface are zero to leading order within the thin-film model. The secondary flow in the liquid film consists of two symmetric recirculation zones, but the magnitude of the secondary flows is approximately 1000 times smaller than that in the core. The liquid film has a finite thickness along the entire perimeter of the tube, indicating that the azimuthal shear stress induced by the secondary flows is strong enough to counteract the tendency of surface tension to redistribute the fluid in the liquid film towards the outer wall.

Having obtained a steady solution at a fixed value of Ca, we use continuation to extend the steady solution branch. Figure 4 shows the behaviour of the computed solutions, characterised by the difference between the film thicknesses on the inner ($\theta = \pi$) and outer ($\theta = 0$) walls, Δh, as a function of the capillary number. At small capillary numbers, the solid part of the solution curve represents solutions for which surface tension is so strong that most of the fluid in the liquid lining is driven towards the outside of the bend, resulting in $\Delta h < 0$. An increase in capillary number corresponds to a reduction in surface tension which allows the azimuthal shear stresses to redistribute more and more fluid towards the inner wall, resulting in an increase in Δh with Ca. The steady symmetric solutions exist for a limited range of Ca and we find a limit point at $Ca \approx 0.1823$, close to the point where the air–liquid interface is approximately centred within the cross-section and $\Delta h \approx 0$. The dashed line in figure 4 represents further (unstable) steady solutions. Along this solution branch the air core continues to move towards the outer wall and appears to approach a solution with zero film thickness on the outer wall at finite capillary number.

In addition, we find a branch of asymmetric solutions that emanates from a supercritical pitchfork bifurcation at $Ca \approx 0.1816$, just before the limit point. Thus, increasing Ca beyond the limit point causes the air core to move towards the outer

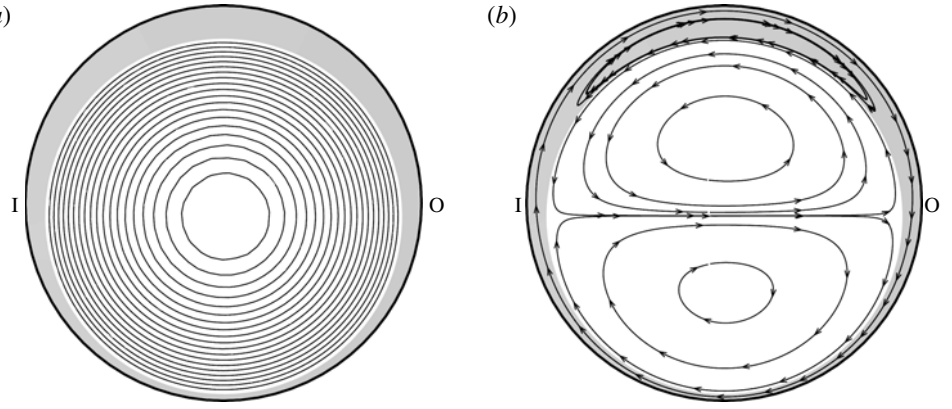

FIGURE 5. Contours of axial velocity (*a*) and secondary-flow streamlines (*b*) for the asymmetric steady state at $Ca = 0.23$ with $\epsilon = 0.1$, $Re = 100$, $\delta = 0.1$, $\rho_2/\rho_1 = 830$ and $\mu_2/\mu_1 = 55$. The region occupied by the lining fluid is shaded.

wall of the tube but also away from the tube's horizontal line of symmetry. There are two conjugate solution branches: one in which the core moves up and the other in which it moves down. Since both solutions have the same value of Δh (which only characterises the core's horizontal position within the tube's cross-section) they cannot be distinguished by the plot in figure 4.

A representative asymmetric solution at $Ca = 0.23$ is illustrated in figure 5, again showing contours of axial velocity (figure 5*a*) and secondary flow streamlines (figure 5*b*). The air core is located nearer the lower wall, but the flow within the core is not significantly changed from that of the symmetric solution shown in figure 3. The secondary flow within the fluid film is somewhat different from that of the symmetric solution, however, with a single asymmetric recirculation zone above the core and streamlines that completely encircle the core, indicating the presence of a net azimuthal flow around the film.

The (inferred) stability of the various steady solutions is confirmed by computing the system's time evolution after a perturbation to the steady state. The symmetric solutions on the lower branch, and the asymmetric solutions that emerge from the pitchfork bifurcation, are indeed stable. In the small region between the pitchfork bifurcation and the limit point, $0.1816 \lesssim Ca \lesssim 0.1823$, indicated by the dotted line in figure 4, the symmetric solution is stable to symmetric perturbations, but unstable to asymmetric perturbations. Beyond the limit point, the symmetric solutions are unstable to any form of perturbation, and the system evolves towards a solution in which a dry spot appears to develop on the outer wall.

3.3. *Parameter studies*

The steady solution structure is robust and is qualitatively unchanged under variations in Re, film thickness, ϵ, and tube curvature, δ. Increasing Re, reducing ϵ or increasing δ all lead to increases in the magnitude of the secondary flows, which shifts the entire solution structure to the left because relatively higher surface tension (lower Ca) is required to balance the increased tangential stresses. In order to understand the origin of the solution structure we next examine the thin-film model developed in § 2.2, which is sufficiently simple to facilitate asymptotic investigation.

4. Analysis of the thin-film model

4.1. *Comparison with Navier–Stokes simulations*

We first demonstrate that the thin-film model developed in § 2.2 does actually reproduce the key features observed in the Navier–Stokes simulations. Our first observation is that the thin-film equation (2.21) has an obvious steady solution in which the film has a constant scaled thickness $\overline{H} = \epsilon\mathscr{C}/\delta$. For a given non-dimensional film thickness ϵ and curvature δ, this solution is realised for a scaled capillary number $\mathscr{C} = \delta/\epsilon$. To compute steady solutions at other capillary numbers we solved the steady equation

$$\mathscr{S}(\overline{H}, \overline{Q}) = \left(-\frac{\delta}{\epsilon}\sin\theta + \frac{\mathrm{d}\overline{H}}{\mathrm{d}\theta} + \frac{\mathrm{d}^3\overline{H}}{\mathrm{d}\theta^3}\right)\overline{H}^3 + \mathscr{C}\sin\theta\overline{H}^2 - \overline{Q} = 0 \tag{4.1}$$

by representing $\overline{H}$ using a Fourier expansion,

$$\overline{H}(\theta) = \sum_{j=0}^{N_f} \overline{H}_j^{[c]}\cos(j\theta) + \sum_{j=1}^{N_f} \overline{H}_j^{[s]}\sin(j\theta), \tag{4.2}$$

and determining the $2N_f + 2$ unknown coefficients $(\overline{H}_0^{[c]}, \ldots, \overline{H}_{N_f}^{[c]}, \overline{H}_1^{[s]}, \ldots, \overline{H}_{N_f}^{[s]}, \overline{Q})$ from the solution of the nonlinear equations

$$\int_0^{2\pi} \mathscr{S}(\overline{H}, \overline{Q})\cos(j\theta)\,\mathrm{d}\theta = 0 \quad \text{for } j = 0, \ldots, N_f, \tag{4.3}$$

$$\int_0^{2\pi} \mathscr{S}(\overline{H}, \overline{Q})\sin(j\theta)\,\mathrm{d}\theta = 0 \quad \text{for } j = 1, \ldots, N_f, \tag{4.4}$$

and the constraint

$$\int_0^{2\pi} \overline{H}\,\mathrm{d}\theta = 2\pi, \tag{4.5}$$

which ensures that the volume of fluid in the liquid film is conserved. The branch of steady solutions is then computed by continuation from the constant-film-thickness solution.

Figure 6 shows a comparison between the steady solution branches computed from simulations of the Navier–Stokes equations and thin-film model for $\epsilon = \delta = 0.01$ and $Re = 100$. We observe excellent qualitative agreement between the bifurcation structures and reasonable quantitative agreement; the relative error in the critical capillary number at the pitchfork bifurcation is approximately 3 %.

4.2. *The stability of the symmetric steady states*

Next we employ the thin-film model to assess the stability of the symmetric steady states that exist for $\mathscr{C} < \delta/\epsilon$. We use the moving-mesh scheme described and validated in Band *et al.* (2009), which is a modified version of the `MOVCOL4` scheme developed by Russell, Williams & Xu (2007). Figures 7(*a*) and 7(*b*) illustrate the evolution of the film thickness $\overline{H}(\theta, t)$ for $\mathscr{C} = 0.01$ and $\delta/\epsilon = 1$, starting from an initial condition close to the stable (lower) symmetric solution branch. The solid lines show the film thickness at $\bar{t} = 10^n$ for $n = 0, 1, \ldots, 6$; we note that the profiles for $\bar{t} = 10^6$ and $\bar{t} = 10^7$ (not shown) are indistinguishable. The film evolves towards a steady state in

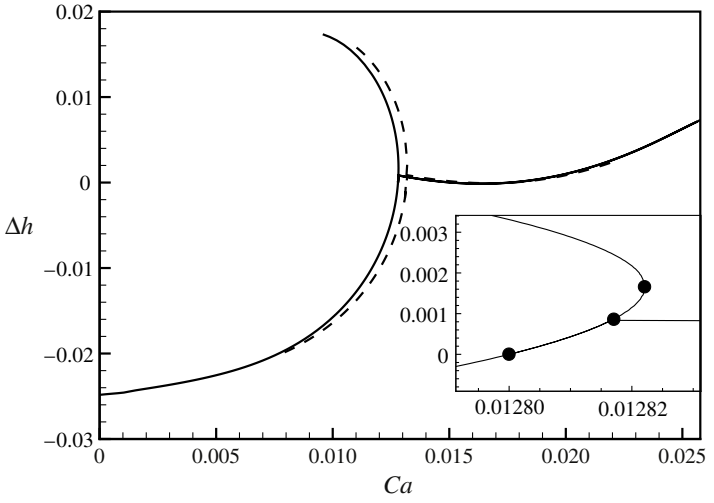

FIGURE 6. Steady solutions of the Navier–Stokes equations (dashed line) and thin-film model (solid line) represented by the difference between the film thickness on the inside and outside of the bend, Δh, plotted against capillary number, Ca. The inset shows a detail of the solution structure (computed with the thin-film model) near the limit point. The markers identify (from left to right) the axisymmetric solution, the bifurcation to the asymmetric solution and the limit point on the symmetric solution branch. The other parameters are fixed at $Re = 100$, $\delta = \epsilon = 0.01$, $\rho_2/\rho_1 = 830$ and $\mu_2/\mu_1 = 55$.

which the film thickness is finite. The film thickness is greatest on the outer wall (at $\theta = 0$) and decreases in the azimuthal direction until a sharp local minimum near $\theta \approx 4\pi/5$; beyond this minimum the film thickness increases rapidly and then remains approximately constant on the inner wall (in the vicinity of $\theta = \pi$).

Figures 7(*c*) and 7(*d*) illustrate the system's behaviour for the same value of δ/ϵ computed using the same scheme, but for an initial condition close to the end of the unstable (upper) solution branch at $\mathscr{C} = 0.77104$; we note that the profiles for $\bar{t} = 10^0$ and $\bar{t} = 10^1$ are indistinguishable. In this case the film thins on the outer wall with a spatial structure similar to the one observed above: in the vicinity of $\theta = 0$ the film thickness only varies very gently; this region is bounded by a sharp local minimum at $\theta \approx \pi/30$ beyond which the film thickness increases towards its maximum on the inner wall (at $\theta = \pi$). However, in this case, the film continues to thin and appears to evolve towards a dry spot on the outer wall.

To explain the difference in the system's behaviour on the two solution branches, we consider the evolution of the film thickness on the outer (or inner) wall when $\overline{H}(\theta = 0, t) \ll 1$ (or $\overline{H}(\theta = \pi, t) \ll 1$). Given that the numerical simulations show that in the thin-film regions the film thickness only varies very gently, we neglect the spatial derivatives in the flux (2.22) and approximate the governing equation (2.21) by

$$\frac{\mathrm{d}\overline{H}}{\mathrm{d}\bar{t}} = \pm\left(\frac{\delta}{\epsilon}\overline{H}^3 - \mathscr{C}\overline{H}^2\right), \tag{4.6}$$

where the plus (minus) sign applies on the outer (inner) wall where $\theta = 0$ ($\theta = \pi$). Hence, if a steady state exists the film thickness on the outer (or inner) wall is either given by $\overline{H}_{unif} = \mathscr{C}\epsilon/\delta$ or by the dry-spot solution $\overline{H} = 0$. The film thickness $\overline{H}_{unif}$ is shown by the horizontal dot-dashed line in figure 7(*a*).

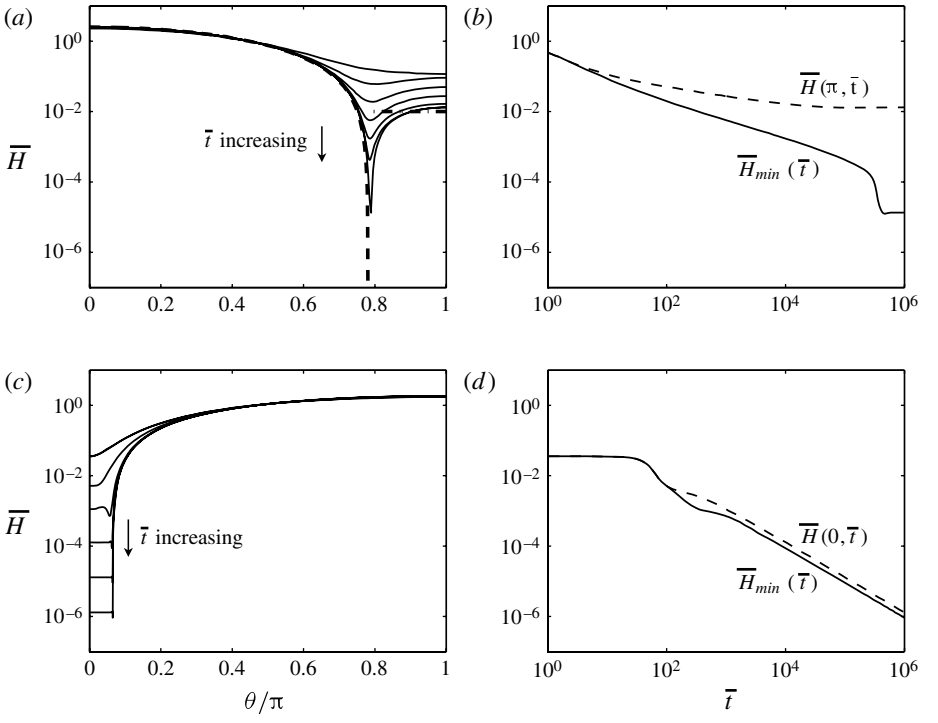

FIGURE 7. Time evolution of the thin-film equation (2.21) for $\delta/\epsilon = 1$ with symmetry boundary conditions at $\theta = 0, \pi$. (*a*,*b*) $\mathscr{C} = 0.01\,(Ca = 0.000128)$, starting from an initial condition close to the stable (lower) symmetric solution branch in figure 6. (*c*,*d*) $\mathscr{C} = 0.77104\,(Ca = 0.00987)$, starting from the initial condition close to the unstable (upper) symmetric solution branch in figure 6. (*a*,*c*) Film thickness $\overline{H}(\theta,\bar{t})$ for $\bar{t} = 10^n$ for $n = 0,\ldots,6$. (*b*,*d*) Time evolution of the minimum film thickness (solid) and the film thickness on the outer (*b*) or inner (*d*) wall (dashed). The horizontal dot-dashed line in (*a*) shows the theoretical prediction for the steady-state film thickness, H_{unif}; the dashed line shows the shape of the steady lobe predicted by (4.9).

To assess the stability of these solutions we note that, for sufficiently thin films, the second term on the right-hand side of (4.6) is greater in magnitude than the first. A straightforward stability analysis based on the approximate equation (4.6) demonstrates that steady solutions on the upper branch (where $\overline{H} \ll 1$ on the outer wall) are unstable; in particular, negative perturbations to the steady finite-thickness solution $\overline{H} = \overline{H}_{unif}$ result in continued thinning of the film with $\overline{H} = O(1/\bar{t})$ as $\bar{t} \to \infty$, i.e. the evolution is towards a dry spot and the asymptotic structure is the same as in the case examined by Band *et al.* (2009). Conversely, perturbations to the steady solution on the lower solution branch (where $\overline{H} \ll 1$ on the inner wall) decay and the system returns to the finite-film thickness solution, $\overline{H} \to \overline{H}_{unif}$ as $\bar{t} \to \infty$.

4.3. *The structure of the steady symmetric solution for* $\mathscr{C} \ll 1$

Even though the presence of the azimuthal shear stress generated by the core flow results in a fundamental change to the behaviour found by Jensen (1997) in the case $\mathscr{C} = 0$, there remain certain similarities to the present case $\mathscr{C} > 0$ on the stable symmetric branch of solutions. In particular, while the film thickness decreases (either to zero or towards a finite value) on the inner wall, the fluid lining the outer wall

redistributes to form a steady lobe of relatively large thickness. For sufficiently small values of the interfacial shear stress (small values of $\mathscr{C}$) the lobe must be bounded by an interface of (approximately) constant mean curvature. Hence for $\mathscr{C} \ll 1$, we expect the steady film thickness in the region occupied by the lobe to be well approximated by $\overline{H} = \overline{h}(\theta)$, where $\overline{h}(\theta)$ satisfies

$$\frac{\mathrm{d}^3\overline{h}}{\mathrm{d}\theta^3} + \frac{\mathrm{d}\overline{h}}{\mathrm{d}\theta} - \frac{\delta}{\epsilon}\sin\theta = 0. \tag{4.7}$$

We follow Jensen (1997) and assume that the symmetric lobe occupies a finite region $|\,\theta\,| < \theta^*$, meeting the wall at $\theta = \theta^*$ with zero apparent contact angle, and that the entire volume of fluid is contained within the lobe. The shape of the lobe can then be determined by solving (4.7) in the region $0 \leqslant \theta \leqslant \theta^*$, subject to the constraints

$$\frac{\mathrm{d}\overline{h}}{\mathrm{d}\theta}(0) = \overline{h}(\theta^*) = \frac{\mathrm{d}\overline{h}}{\mathrm{d}\theta}(\theta^*) = 0 \quad \text{and} \quad \int_0^{\theta^*} \overline{h}(\theta)\,\mathrm{d}\theta = \pi. \tag{4.8}$$

The solution is given by

$$\overline{h}(\theta) = \frac{\delta}{2\epsilon}(\cos\theta^* + \theta^*\mathrm{cosec}\,\theta^* - (1 + \theta^*\cot\theta^*)\cos\theta - \theta\sin\theta), \tag{4.9}$$

where θ^* is the unique root of the equation

$$\theta^*\cos\theta^* + (\theta^*)^2\,\mathrm{cosec}\,\theta^* - 2\sin\theta^* = \frac{2\pi\epsilon}{\delta}. \tag{4.10}$$

This is the same as Jensen's (1997) solution for the lobe shape when $\mathscr{C} = 0$. In this case ($\mathscr{C} = 0$), the thin-film region on the inner wall continues to thin indefinitely while the lobe remains approximately steady, whereas for $\mathscr{C} > 0$ the thin-film region also approaches a steady state. We note that it is possible to employ matched asymptotic expansions to match the solution (4.9) for the film thickness in the lobe region to the constant-thickness solution on the inner wall (where $\overline{H} = \overline{H}_{unif}$). This requires the use of two intermediate regions to describe the behaviour in the vicinity of the sharp minimum in the film thickness shown in figure 7(*a*). The matching provides the formal justification for assuming a zero apparent contact angle at $\theta = \theta^*$ and is described briefly in the Appendix. Here we simply note that figure 7(*a*) demonstrates that $\overline{h}(\theta)$ (represented by the dashed line) provides an excellent prediction for the steady film thickness on the outer wall.

4.4. *Weakly nonlinear analysis*

Finally, we employ the thin-film model to analyse the solution structure in the vicinity of the limit point on the symmetric solution branch shown in figure 6. For this purpose we consider (2.21) in the regime in which $0 < \delta/\epsilon \ll 1$. As already noted, when $\mathscr{C} = \delta/\epsilon$, the equations admit the uniform solution $\overline{H} = 1$ and the numerical evidence indicates that the uniform solution, limit point and pitchfork bifurcation all occur within a very small range of $\mathscr{C}$; see figure 6. In the static, straight-tube limit in which $\mathscr{C} = \delta/\epsilon \to 0$, the translational degeneracy of the interface position means that the uniform solution is neutrally stable. For small, but finite, values of δ/ϵ and $\mathscr{C}$, the uniform solution is near-neutrally stable and we can develop a weakly nonlinear analysis using its near-neutral eigenfunctions to explore the nearby solution structure.

We consider the linear stability of the uniform state by posing $\overline{H} = 1 + (\delta/\epsilon)\widehat{H}_1(\theta, t)$, which gives the equation governing the perturbation as

$$\frac{\partial \widehat{H}_1}{\partial \bar{t}} + \mathscr{L}\widehat{H}_1 = 0, \tag{4.11}$$

where

$$\mathscr{L} = \frac{\partial^2}{\partial\theta^2} + \frac{\partial^4}{\partial\theta^4}. \tag{4.12}$$

Equation (4.11) admits solutions of the form $\widehat{H}_1 = A\cos\theta + B\sin\theta$, where A and B are constants, which corresponds to a rigid-body displacement of the interface (the translational degeneracy), and the solution is neutrally stable (to this order). We next consider a small perturbation to $\mathscr{C} = \delta/\epsilon$, and determine the evolution of perturbations to the uniform solution on the long time scale $\bar{t} = (\epsilon^2/\delta^2)\,T$. Specifically, we consider

$$\mathscr{C} = \frac{\delta}{\epsilon} + \frac{\widehat{\mathscr{C}}}{576}\frac{\delta^3}{\epsilon^3}, \tag{4.13}$$

where $\widehat{\mathscr{C}}$ is a measure of the deviation from the uniform state, and seek solutions of the form

$$\overline{H} = 1 + \frac{\delta}{\epsilon}\overline{H}_1(\theta, T) + \frac{\delta^2}{\epsilon^2}\overline{H}_2(\theta, T) + \cdots. \tag{4.14}$$

As expected, at $O(\delta/\epsilon)$ we find $\mathscr{L}\overline{H}_1 = 0$, which has solution

$$\overline{H}_1 = A(T)\cos\theta + B(T)\sin\theta, \tag{4.15}$$

where the amplitude functions $A(T)$ and $B(T)$ will be determined at higher order.

At $O(\delta^2/\epsilon^2)$, the governing equation is

$$\mathscr{L}\overline{H}_2 = \frac{\partial}{\partial\theta}(\overline{H}_1\sin\theta), \tag{4.16}$$

which has solution

$$\overline{H}_2 = \tfrac{1}{12}A(T)\cos(2\theta) + \tfrac{1}{12}B(T)\sin(2\theta). \tag{4.17}$$

At $O(\delta^3/\epsilon^3)$, the governing equation is $\mathscr{L}\overline{H}_3 = \mathscr{F}$, where

$$\mathscr{F} = -\frac{\mathrm{d}\overline{H}_1}{\mathrm{d}T} + \frac{\partial}{\partial\theta}\left(\sin\theta(\overline{H}_2 + 2\overline{H}_1^2) - 3\overline{H}_1\left(\frac{\partial\overline{H}_2}{\partial\theta} + \frac{\partial^3\overline{H}_2}{\partial\theta^3}\right) - \frac{\widehat{\mathscr{C}}}{576}\sin\theta\right). \tag{4.18}$$

The Fredholm alternative theorem states that a solution $\overline{H}_3$ exists if and only if

$$\int_0^{2\pi}\mathscr{F}\cos\theta\,\mathrm{d}\theta = \int_0^{2\pi}\mathscr{F}\sin\theta\,\mathrm{d}\theta = 0, \tag{4.19}$$

because the differential operator $\mathscr{L}$ is self-adjoint. We use (4.19) to eliminate secular terms, and obtain the following coupled amplitude evolution equations:

$$\frac{\mathrm{d}A}{\mathrm{d}T} = \frac{3}{4}B^2 - \frac{1}{4}A^2 - \frac{1}{24}A - \frac{\widehat{\mathscr{C}}}{576}, \quad \frac{\mathrm{d}B}{\mathrm{d}T} = -B\left(A + \frac{1}{24}\right). \tag{4.20}$$

These equations describe a (truncated) normal form associated with an unfolded, codimension-two point known as a fold-Hopf, saddle-node-Hopf or

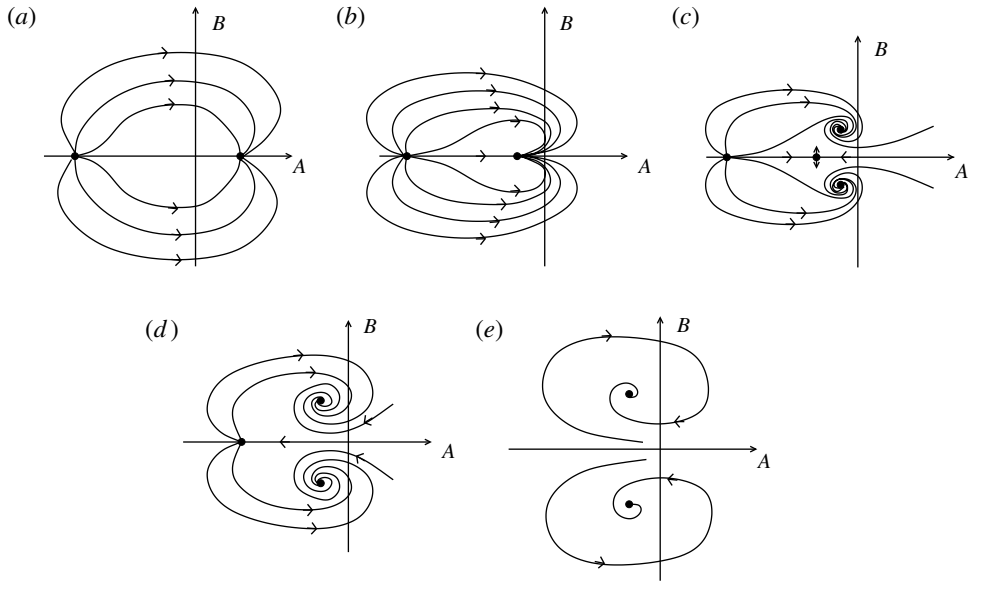

FIGURE 8. Sketch of the dynamics in the phase plane corresponding to the amplitude equations (4.20) for (*a*) $\widehat{\mathscr{C}} < 3/4$, (*b*) $\widehat{\mathscr{C}} = 3/4$, (*c*) $3/4 < \widehat{\mathscr{C}} < 1$, (*d*) $\widehat{\mathscr{C}} = 1$, (*e*) $\widehat{\mathscr{C}} > 1$. Solutions that lie on the horizontal axis are symmetric.

Guckenheimer–Garilov bifurcation (see *e.g* Kuznetsov 1998). In the present context, the codimension-two point corresponds to the translational degeneracy in the straight tube limit at which symmetric and antisymmetric neutral modes coexist. The initial perturbation in the normal form is then induced by the weak curvature.

Equations (4.20) admit the steady-state solutions

$$(A, B) = \left(\frac{-1 \pm \sqrt{1 - \widehat{\mathscr{C}}}}{12}, 0 \right), \left(-\frac{1}{24}, \pm \frac{1}{\sqrt{432}} \left(\widehat{\mathscr{C}} - \frac{3}{4} \right)^{1/2} \right), \tag{4.21}$$

and the phase plane can be classified according to the value of $\widehat{\mathscr{C}}$, as illustrated by figure 8. For $\widehat{\mathscr{C}} < 3/4$, figure 8(*a*), there are two symmetric ($B = 0$) equilibrium solutions: one stable node and one unstable node. The case $\widehat{\mathscr{C}} = 0$ shows that the uniform-film solution is the stable node, in agreement with the numerical simulations. The case $\widehat{\mathscr{C}} = 3/4$, figure 8(*b*), corresponds to the pitchfork bifurcation where the stable node becomes degenerate with a zero eigenvalue. In the region $3/4 < \widehat{\mathscr{C}} < 1$, figure 8(*c*), there are two stable foci, the asymmetric equilibria, an unstable symmetric node and a symmetric saddle. At $\widehat{\mathscr{C}} = 1$, figure 8(*d*), the unstable node and saddle annihilate each other in a saddle-node (limit point) bifurcation. Finally, for $\widehat{\mathscr{C}} > 1$, figure 8(*e*), there remain only two stable asymmetric foci.

The weakly nonlinear analysis thus reproduces the sequence of events observed in both the Navier–Stokes and thin-film simulations under reduction in surface tension (increase in Ca or $\mathscr{C}$): a stable (approximately) uniform-film solution, followed by a symmetry-breaking pitchfork bifurcation and then a limit point on the symmetric solution branch. Moreover, the prediction that the distance between the uniform

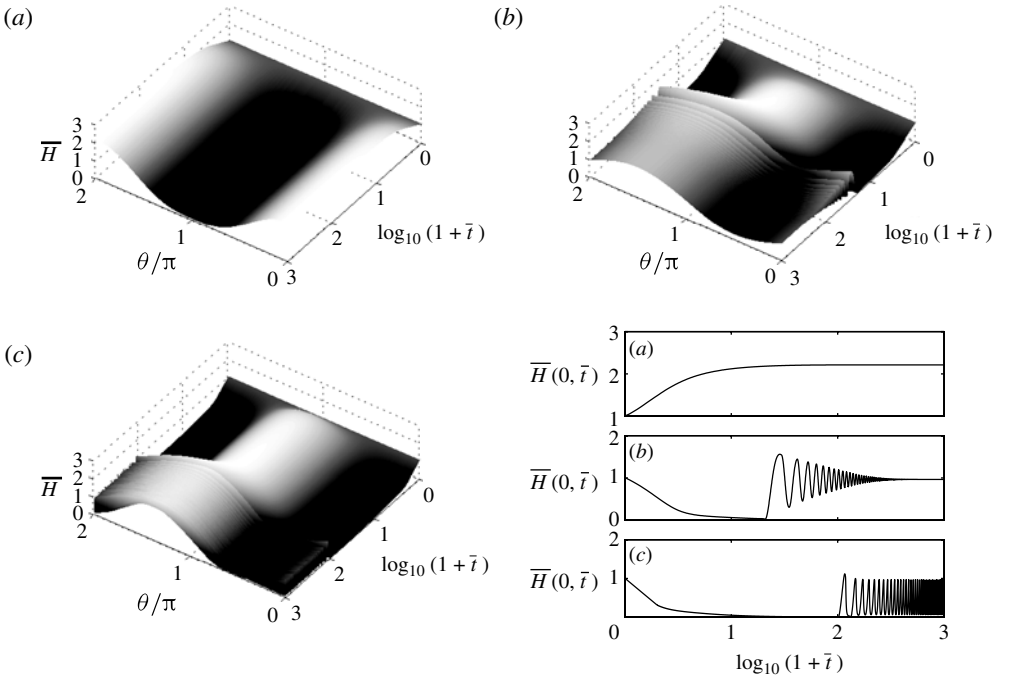

FIGURE 9. Time evolution of the thin-film equation (2.21) with periodic boundary conditions from a small perturbation to $\overline{H} = 1$ for $\delta/\epsilon = 1$ and (*a*) $\mathscr{C} = 0.5$, (*b*) $\mathscr{C} = 1.5$, (*c*) $\mathscr{C} = 2.1$, computed using the finite difference scheme described and validated in Band *et al.* (2009). (The scheme is second-order accurate in space and uses MATLAB's `ODE15s` to time step.)

solution and pitchfork bifurcation is three times the distance between the bifurcation and the limit point is in quantitative agreement with the numerical results for the thin-film model shown in the inset in figure 6, despite the fact that $\delta/\epsilon = 1$ in this case. In addition, the analysis reveals that the asymmetric solutions are foci, suggesting that the time evolution towards these states will be oscillatory. This behaviour is confirmed by simulating the time evolution of the film thickness at three values of $\mathscr{C}$ following a perturbation of the uniform state. Figure 9(*a*) shows that for $\mathscr{C} = 0.5$ (below the pitchfork bifurcation) the system evolves monotonically towards the stable, steady symmetric solution for which the point of minimum film thickness is on the inner wall at $\theta = \pi$. For $\mathscr{C} = 1.5$, beyond the pitchfork bifurcation, figure 9(*b*) shows that the system initially approaches the symmetric draining solution (with the minimum film thickness on the outer wall at $\theta = 0$), but then evolves towards the steady asymmetric solution in an oscillatory fashion, as predicted. Finally, for $\mathscr{C} = 2.1$, again after a long, near-symmetric evolution, the system develops a sustained limit cycle oscillation (see figure 9*c*), which presumably arises through a Hopf bifurcation from the asymmetric solution, as found in the normal form analysis presented by Kuznetsov (1998).

A similar oscillatory evolution to the asymmetric steady state is also observed in the Navier–Stokes simulations, but we were unable to compute the evolution towards the limit cycle because we could not resolve the extremely thin films that occur before the limit cycle develops; see figure 9(*c*).

5. Discussion

In this paper, we have investigated a particular two-phase flow in which an air core surrounded by an immiscible, liquid film is driven though a rigid, curved tube by a constant imposed axial pressure gradient. The system is a simplified model for the flow in the conducting airways of the lung. In the limit when the film is thin compared to the radius of the tube, Jensen (1997) showed that, in the absence of core flow, there is no stable steady solution of finite-film thickness and the air core continually moves towards the inner wall of the bend approaching a 'dry spot' steady solution. Also in the thin-film limit, Band *et al.* (2009) showed that no steady solution of finite-film thickness is possible if a stress distribution corresponding to the core flow in a curved tube is imposed at the air–liquid interface of a film lining a straight cylindrical tube. In the latter case, however, the air core is driven towards what would be the outer wall of the curved tube. The principal aim of the present work was to examine the behaviour of the system when both centreline curvature and a core flow are present. The relative importance of the core flow is governed by a capillary number, Ca, which we interpret as the ratio of the magnitude of the driving pressure gradient relative to the pressure difference induced by surface tension acting at the curved air–liquid interface.

Using simulations of the Navier–Stokes equations and a thin-film model, we demonstrated that it is possible to find steady solutions of finite-film thickness in which the tangential stresses imposed by the secondary flows in the core are exactly balanced by the surface-tension-driven flows induced by the non-uniform curvature of the air–liquid interface. Indeed, we find an entire family of steady solutions that are symmetric about the plane containing the tube's centreline. These symmetric steady solutions lose stability through a limit point at finite Ca and the solutions on the upper (unstable) branch then approach the 'dry spot' solution of Band *et al.* (2009), where the branch terminates. This solution branch will always exist, provided that the secondary flows are of standard Dean (1928) form and that the tube has non-negligible centreline curvature.

In addition, we find a branch of asymmetric solutions arising from a pitchfork bifurcation that occurs shortly before the limit point in the symmetric solution branch. The asymmetric solutions persist for values of Ca beyond the limit point in the symmetric-solution branch, and appear to approach an asymmetric 'dry spot' solution. A weakly nonlinear analysis of the thin-film equations showed that the bifurcation structure arises from a particular degeneracy present in a perfectly straight tube: a cylindrical air–liquid interface can be located anywhere within the tube's cross-section. The degeneracy can be interpreted as a codimension-two point at which both symmetric and antisymmetric neutral eigenfunctions are present. The unfolding of this so-called saddle-node-pitchfork bifurcation by adding weak centreline curvature explains the origin of the observed solution structure.

In order to reduce the complexity of the model, we have neglected the effects of gravity and have not considered any axial variations in the system. Weak gravity acting in any direction other than the plane containing the tube's centreline will unfold the pitchfork bifurcation into a single connected stable solution branch and a disconnected branch that loses stability through a limit point, but will not dramatically change the observed behaviour. Gravity acting in the plane of the tube's centreline will not alter the solution structure, but will alter the critical values depending on whether it acts to enhance or oppose the surface-tension-driven flow. Jensen (1997) showed that the thin-film system can be unstable to axial perturbations in the absence of core flow, and related core-annular flows in straight tubes are known to exhibit a wide variety of instabilities in the axial direction (Joseph *et al.* 1997). We expect all these instabilities

to occur in the present system, but have not attempted to determine their location in the solution structure. We have also neglected the dynamic role of surfactant, assuming the surface tension to be constant. In fact, the interaction of insoluble surfactant and interfacial shear can lead to new mechanisms of instability, as shown by Halpern & Frenkel (2003). For core-annular flow in straight tubes, Wei & Rumschitzki (2005) have demonstrated that Marangoni forces induced by the redistribution of insoluble surfactant by an interfacial shear can destabilise or stabilise the interface depending on the parameter regime. It is likely, therefore, that the presence of surfactant will affect the critical capillary numbers determined in the present study.

The calculated solution structure depends on the form of the core flow, for which the standard two-vortex (Dean 1928) flow is not necessarily the only possibility. The flow of a single fluid in a curved pipe has been extensively studied; see reviews in Pedley (1980), Berger, Talbot & Yao (1983) and Ito (1987). The main governing parameter is the Dean number, $D = 2Re\sqrt{2\delta}$, and a large number of alternative solutions exist at large Dean number (Daskopoulos & Lenhoff 1989). In the single-phase problem, the alternative solutions appear to be disconnected branches, suggesting that these branches will remain disconnected in the two-phase problem. Furthermore, in the physiological context, these flows are likely to be realised only in the very largest airways. Nonetheless, complete characterisation of the solution structure, even in single-phase flow, remains an open problem.

Our assumption of a steady driving pressure gradient is only appropriate if the time scale for fluid redistribution is much faster than that of the breathing cycle. When the driving pressure gradient is unsteady and of sufficiently high frequency, the core flow will be modified (see Lyne 1971, Siggers & Waters 2008 and references therein), and steady solutions are not possible. Siggers & Waters (2008) observed complex behaviour of the periodic solutions for single-phase flow in a curved pipe driven by an oscillatory pressure gradient. The complete characterisation of these solutions and their relation to those in the two-phase problem remain challenges for the future.

M.H. and A.L.H. would like to acknowledge the contributions of Benjamin Metz and Luigi Colucci to the development of `oomph-lib`'s unstructured meshing and re-meshing capabilities. S.L.W. is grateful to EPSRC for funding in the form of an Advanced Research Fellowship. Finally, the authors would like to dedicate this work to Professor T. J. Pedley on the occasion of his 70th birthday. As his research students, M.H., S.L.W. and A.L.H. were all supported, guided and inspired by Tim to pursue research careers in biological fluid mechanics. Thank you.

Appendix. Details of the matching process for the symmetric, steady thin-film solution

In this appendix we describe the two intermediate regions near $\theta = \theta^*$ required to match the leading-order lobe and inner-wall solutions in § 4.3 in the symmetric-steady-state regime in which the film thickness $\overline{H}(\theta)$ is governed by (4.1), with $\overline{Q} = 0$ and $\delta/\epsilon = O(1)$ as $\mathscr{C} \to 0$.

A local analysis of the leading-order lobe solution (4.6) near the apparent contact point $\theta = \theta^*$ shows that $\overline{h}(\theta) \sim \mathscr{A}(\theta - \theta^*)^2$ as $\theta \uparrow \theta^*$, where $\mathscr{A} = \delta(\theta^*\mathrm{cosec}\,\theta^* - \cos\theta^*)/4\epsilon$ is a positive constant, the lobe having zero contact angle at $\theta = \theta^*$. Thus, the leading-order lobe solution (4.6) (valid for $0 < \theta < \theta^*$) does not match directly with the leading-order solution $\overline{H}_{unif} = \mathscr{C}\epsilon/\delta$ in the thin-film region (in which $\theta^* < \theta < \pi$). The matching requires two intermediate regions, in both of which the

resulting boundary value problems for the film thickness are exactly the same as in § 2.8 of King & Bowen (2001), with $n = 1$ in their notation. The matching is therefore the same as in King & Bowen (2001), while numerical solutions of the two boundary value problems are reported in Bowen (1998), so we describe here only the relevant scalings and new physics.

In the first intermediate region, the previously neglected tangential shear stress enters: there is a balance between the third and fourth terms in $\mathscr{S}(\overline{H}, 0)$ in (4.1) and matching with the leading-order solution (4.6) in the lobe leads to the scalings

$$\theta = \theta^* + \frac{\mathscr{C} \sin\theta^*}{\mathscr{A}^2}\xi, \quad \overline{H} = \frac{\mathscr{C}^2 \sin^2\theta^*}{\mathscr{A}^3}\eta. \tag{A 1}$$

Here, we have introduced the constants $\mathscr{A}$ and $\sin\theta^*$ to simplify the resulting boundary value problem for $\eta(\xi)$, the rescaled film thickness, which, at leading order in $\mathscr{C}$, is given by

$$\eta\frac{\mathrm{d}^3\eta}{\mathrm{d}\xi^3} = -1 \text{ for } -\infty < \xi < \infty, \quad \eta \sim \xi^2 \text{ as } \xi \to -\infty, \quad \eta \sim \left(\frac{8}{3}\right)^{1/2}\xi^{3/2} \text{ as } \xi \to \infty, \tag{A 2}$$

where the boundary condition at $\xi = \infty$ follows from matching with the second intermediate region below. As reported in King & Bowen (2001), $\eta(\xi)$ is uniquely determined up to translations in ξ. The numerical solution in Bowen (1998) shows that the film thickness has a unique minimum in this region. The rapid change in curvature is supported at leading order by the shear stress exerted on the free surface by the secondary flow in the core.

In the second intermediate region, the axial curvature of the interface again plays a role: there is now a balance between the first, third and fourth terms in $\mathscr{S}(\overline{H}, 0)$ in (4.1) and matching with the leading-order solution in the thin-film region leads to the scalings

$$\theta = \theta^* + \left(\frac{\epsilon^2\mathscr{C}}{\delta^2 \sin\theta^*}\right)^{1/3}\widehat{\xi}, \quad \overline{H} = \overline{H}_{unif}\,\widehat{\eta}, \tag{A 3}$$

where $\overline{H}_{unif} = \mathscr{C}\epsilon/\delta$ is the uniform-film-thickness solution determined in § 4.1. Here, we have again scaled both the dependent and independent variables in order to simplify the resulting boundary value problem for $\widehat{\eta}(\widehat{\xi})$, which, at leading order in $\mathscr{C}$, is given by

$$\widehat{\eta}\frac{\mathrm{d}^3\widehat{\eta}}{\mathrm{d}\widehat{\xi}^3} = \widehat{\eta} - 1 \text{ for } \widehat{\xi} > 0, \quad \widehat{\eta} \sim \left(\frac{8}{3}\right)^{1/2}\widehat{\xi}^{3/2} \text{ as } \widehat{\xi} \to 0, \quad \widehat{\eta} \to 1 \text{ as } \widehat{\xi} \to \infty, \tag{A 4}$$

where the boundary condition at $\widehat{\xi} = 0$ follows from matching with the first intermediate region above. As reported in King & Bowen (2001), the film thickness $\widehat{\eta}(\widehat{\xi})$ is uniquely determined. The numerical solution in Bowen (1998) shows that, as $\widehat{\xi}$ increases from $\widehat{\xi} = 0$ to $\widehat{\xi} = \infty$, the film thickness initially overshoots the far-field value of unity by a factor of approximately six. The far-field value is attained after some much smaller capillary ripples that arise because the competing effects of centre-line curvature and of the secondary flow are felt at leading order in this region.

REFERENCES

BAND, L. R., RILEY, D. S., MATTHEWS, P. C., OLIVER, J. M. & WATERS, S. L. 2009 Annular thin-film flows driven by azimuthal variations in interfacial tension. *Q. J. Mech. Appl. Math.* **62** (4), 403–430.

BERGER, S. A., TALBOT, L. & YAO, L.-S. 1983 Flow in curved tubes. *Annu. Rev. Fluid Mech.* **15**, 461–512.

BOWEN, M. 1998 High order diffusion. PhD thesis, University of Nottingham.

CAIRNCROSS, R. A., SCHUNK, P. R., BAER, T. A., RAO, R. R. & SACKINGER, P. A. 2000 A finite element method for free surface flows of incompressible fluids in three dimensions. Part I. Boundary fitted mesh motion. *Intl J. Numer. Meth. Fluids* **33**, 375–403.

DASKOPOULOS, P. & LENHOFF, A. M. 1989 Flow in curved ducts: bifurcation structure for stationary ducts. *J. Fluid Mech.* **203**, 125–148.

DEAN, W. R. 1928 The stream-line motion of fluid in a curved pipe. *Phil. Mag.* **5**, 673–695.

GRESHO, P. M. & SANI, R. L. 1998 *Incompressible Flow and the Finite Element Method, vol. 1, Advection–Diffusion and Isothermal Laminar Flow*. Wiley.

HALPERN, D. & FRENKEL, A. L. 2003 Destabilization of a creeping flow by interfacial surfactant: linear theory extended to all wavenumbers. *J. Fluid Mech.* **485**, 191–220.

HEIL, M. & HAZEL, A. L. 2006 `oomph-lib`: an object-oriented multi-physics finite-element library. In *Fluid–Structure Interaction* (ed. M. Schäfer & H.-J. Bungartz), Lecture Notes on Computational Science and Engineering, pp. 19–49. Springer. `oomph-lib` is available as open-source software at http://www.oomph-lib.org.

ITO, H. 1987 Flow in curved pipes. *JSME Intl J.* **30** (262), 543–552.

JENSEN, O. E. 1997 The thin liquid lining of a weakly curved cylindrical tube. *J. Fluid Mech.* **331**, 373–403.

JOSEPH, D. D., BAI, R., CHEN, K. P. & RENARDY, Y. Y. 1997 Core-annular flows. *Annu. Rev. Fluid Mech.* **29**, 65–90.

KING, J. R. & BOWEN, M. 2001 Moving boundary problems and non-uniqueness for the thin film equation. *Eur. J. Appl. Math.* **12**, 321–356.

KUZNETSOV, Y. A. 1998 *Elements of Applied Bifurcation Theory*, 2nd edn. Berlin, Springer.

LYNE, W. H. 1971 Unsteady viscous flow in a curved pipe. *J. Fluid Mech.* **45**, 13–31.

MYERS, T. G. 1998 Thin films with high surface tension. *SIAM Rev.* **40**, 441–462.

ORON, A., DAVIS, S. H. & BANKOFF, S. G. 1997 Long-scale evolution of thin liquid films. *Rev. Mod. Phys.* **69**, 931–980.

PEDLEY, T. J. 1977 Pulmonary fluid dynamics. *Annu. Rev. Fluid Mech.* **9**, 229–274.

PEDLEY, T. J. 1980 *The Fluid Mechanics of Large Blood Vessels*. Cambridge University Press.

RUSCHAK, K. J. 1980 A method for incorporating free boundaries with surface tension in finite element fluid-flow simulators. *Intl J. Numer. Meth. Engng* **15**, 639–648.

RUSSELL, J. R. D., WILLIAMS, J. F. & XU, X. 2007 MOVCOL4: a moving mesh code for fourth-order time-dependent partial differential equations. *SIAM J. Sci. Comput.* **29** (1), 197–320.

SHEWCHUK, J. R. 1996 Engineering a 2D quality mesh generator and Delaunay triangulator. In *Applied Computational Geometry: Towards Geometric Engineering* (ed. M. C. Lin & D. Manocha). *Lecture Notes in Computer Science*, vol. 1148. pp. 203–222. Springer.

SIGGERS, J. H. & WATERS, S. L. 2008 Unsteady flows in pipes with finite curvature. *J. Fluid Mech.* **600**, 133–165.

WEI, H.-H. & RUMSCHITZKI, D. S. 2005 The effects of insoluble surfactants on the linear stability of a core-annular flow. *J. Fluid Mech.* **541**, 115–142.

ZIENKIEWICZ, O. C. & ZHU, J. Z. 1992 The superconvergent patch recovery and a posteriori error estimates. Part 1. The recovery technique. *Intl J. Numer. Meth. Engng* **33** (7).